Energy & Environmental Science

ROYAL SOCIETY OF CHEMISTRY

PAPER

View Article Online
View Journal | View Issue

Cite this: *Energy Environ. Sci.*, 2021, **14**, 1449

High-performance ammonia oxidation catalysts for anion-exchange membrane direct ammonia fuel cells†

Yi Li,‡[ab] Hemanth Somarajan Pillai,‡[c] Teng Wang,‡[d] Sooyeon Hwang,‡[e] Yun Zhao,[d] Zhi Qiao,[a] Qingmin Mu,[c] Stavros Karakalos,[f] Mengjie Chen,[a] Juan Yang,*[b] Dong Su,[e] Hongliang Xin,*[c] Yushan Yan*[d] and Gang Wu*[a]

Low-temperature direct ammonia fuel cells (DAFCs) use carbon-neutral ammonia as a fuel, which has attracted increasing attention recently due to ammonia's low source-to-tank energy cost, easy transport and storage, and wide availability. However, current DAFC technologies are greatly limited by the kinetically sluggish ammonia oxidation reaction (AOR) at the anode. Herein, we report an AOR catalyst, in which ternary PtIrZn nanoparticles with an average size of 2.3 ± 0.2 nm were highly dispersed on a binary composite support comprising cerium oxide (CeO_2) and zeolitic imidazolate framework-8 (ZIF-8)-derived carbon (PtIrZn/CeO_2-ZIF-8) through a sonochemical-assisted synthesis method. The PtIrZn alloy, with the aid of abundant OH_{ad} provided by CeO_2 and uniform particle dispersibility contributed by porous ZIF-8 carbon (surface area: ~600 m^2 g^{-1}), has shown highly efficient catalytic activity for the AOR in alkaline media, superior to that of commercial PtIr/C. The rotating disk electrode (RDE) results indicate a lower onset potential (0.35 *vs.* 0.43 V), relative to the reversible hydrogen electrode at room temperature, and a decreased activation energy (~36.7 *vs.* 50.8 kJ mol^{-1}) relative to the PtIr/C catalyst. Notably, the PtIrZn/CeO_2-ZIF-8 catalyst was assembled with a high-performance hydroxide anion-exchange membrane to fabricate an alkaline DAFC, reaching a peak power density of 91 mW cm^{-2}. Unlike in aqueous electrolytes, supports play a critical role in improving uniform ionomer distribution and mass transport in the anode. PtIrZn nanoparticles on silicon dioxide (SiO_2) integrated with carboxyl-functionalized carbon nanotubes (CNT–COOH) were further studied as the anode in a DAFC. A significantly enhanced peak power density of 314 mW cm^{-2} was achieved. Density functional theory calculations elucidated that Zn atoms in the PtIr alloy can reduce the theoretical limiting potential of *NH_2 dehydrogenation to *NH by ~0.1 V, which can be attributed to a Zn-modulated upshift of the Pt–Ir d-band that facilitates the N–H bond breakage.

Received 21st October 2020,
Accepted 14th January 2021

DOI: 10.1039/d0ee03351k

rsc.li/ees

Broader context

The development of clean hydrogen fuel cells is crucial for energy and environment sustainability, but we still face grand challenges in terms of difficulties of hydrogen production, transportation, distribution, and storage. Alternatively, ammonia, a carbon-neutral fuel, is an ideal hydrogen carrier, which can be readily transported and stored using existing infrastructures, and then directly utilized for energy applications through a direct ammonia fuel cell (DAFC). However, the kinetically sluggish ammonia oxidation reaction (AOR) in DAFCs requires substantial precious metal catalysts (*e.g.*, Pt and Ir), leading to prohibitively high cost. This research is dedicated to reducing the cost of DAFCs by developing advanced AOR catalysts with reduced precious metal loadings and improved catalytic performance. High-performance DAFCs in the future can provide power sources without CO_2 emission for a variety of applications, including electric vehicles, portable electronics, and stationary residencies.

[a] *Department of Chemical and Biological Engineering, University at Buffalo, The State University of New York, Buffalo, NY 14260, USA. E-mail: gangwu@buffalo.edu*
[b] *School of Materials Science and Engineering, Jiangsu University, Zhenjiang, 212013, China. E-mail: yangjuan6347@ujs.edu.cn*
[c] *Department of Chemical Engineering, Virginia Polytechnic Institute and State University, Blacksburg, Virginia 24061, USA. E-mail: hxin@vt.edu*
[d] *Department of Chemical and Biomolecular Engineering, Center for Catalytic Science and Technology, University of Delaware, Newark, DE 19716, USA. E-mail: yanys@udel.edu*
[e] *Center for Functional Nanomaterials, Brookhaven National Laboratory, Upton, New York 11973, USA*
[f] *Department of Chemical Engineering, University of South Carolina, Columbia, South Carolina 29208, USA*

† Electronic supplementary information (ESI) available. See DOI: 10.1039/d0ee03351k

‡ These authors contributed equally.

1. Introduction

Hydrogen is a promising and sustainable fuel since it only produces water when consumed by a fuel cell. It can be produced through water-splitting by utilizing renewable and clean solar and wind electricity.[1,2] However, the advent of the hydrogen economy cannot be realized until technical barriers related to hydrogen transportation, distribution, and storage are overcome. Alternatively, the concept of an ammonia (NH_3) economy has recently gained eminence due to the following reasons.[3–6] First, ammonia as a cost-effective hydrogen carrier and carbon-free fuel is in a liquid state at near ambient conditions, and it enables a complete cycle of synthesis and consumption that would not produce greenhouse gas emissions. Second, the infrastructure and supply chain for ammonia as a transport fuel is already in existence or can be easily modified. Third, dissociating ammonia for hydrogen generation and then using the hydrogen in a fuel cell or a direct ammonia input to a fuel cell can be realized for electricity generation as a power source with high energy density for transportation applications.[1,7,8] In particular, low-temperature direct ammonia fuel cells (DAFCs) can directly utilize ammonia at the anode, which has great promise for vehicle applications, because of its fast start-up superiority in comparison to high-temperature DAFCs (*e.g.*, ammonia-fueled solid oxide fuel cells, SOFCs, and protonic ceramic fuel cells, PCFCs).[7,9,10] Nevertheless, the development of DAFCs is at an earlier stage when compared with hydrogen fuel cells. This is mainly due to the more complex and sluggish anodic ammonia oxidation reaction (AOR) than the hydrogen oxidation reaction (HOR).[11]

Earlier research indicated that Pt, Ir, and their alloys can catalyze the AOR in alkaline media at low temperature.[12,13] The standard potential of the AOR is −0.77 V *vs.* SHE (0.056 V *vs.* RHE), very close to that of the hydrogen oxidation reaction at −0.83 V (0 V *vs.* RHE) in alkaline media at 25 °C. However, the overpotential on Pt-based catalysts at room temperature is larger than 0.40 V, which significantly reduces the energy conversion efficiency for DAFC applications.[13,14] Accordingly, it is anticipated that the AOR could commence in the hydrogen zone (0 to 0.40 V *vs.* RHE) if a more efficient catalyst was used. The modulation of the *H oxidation potential is a way to design an efficient AOR catalyst. It was reported that the hydrogen adsorption could be suppressed by incorporating Pt with high hydrogen-overpotential metals (*e.g.*, Zn).[15,16] Therefore, the knowledge gained from Pt–Zn alloys provides a guide in this work to explore ternary Pt–Ir–Zn alloys for the AOR. Also, our density functional theory calculations predicted that Zn atoms in the PtIr alloy could reduce the theoretical limiting potential of $*NH_2$ dehydrogenation to *NH because a Zn-modulated upshift of the Pt–Ir d-band facilitates the N–H bond breakage. Driven by the theoretical understanding, we synthesized a new PtIrZn ternary catalyst for the AOR.

Besides, catalyst supports play a critical role in uniformly dispersing metal nanoparticles, improving catalyst utilization, and offering a unique metal–support interaction for intrinsic activity enhancement. Our previous report has demonstrated that silicon dioxide (SiO_2) and carboxyl functionalized carbon nanotubes (CNT–COOH) as a composite support can be used for effective Pt alloy nanoparticle deposition.[13] The interfaces between SiO_2 and Pt alloys facilitate the AOR activity because SiO_2 could supply abundant OH_{ad} to the nearby metallic catalytic sites.[17] However, the nanoparticle dispersion on this composite support is not very uniform.[13] Therefore, improving the nanoparticle dispersion has allured us to develop a novel composite support in this work. In light of this, cerium oxide (CeO_2) and zeolitic imidazolate framework-8 (ZIF-8)-derived carbon were newly explored for the PtIrZn nanoparticle catalyst. CeO_2 is widely used to support metal nanoparticles because the Ce^{3+} in CeO_2 can work as a Lewis base to modify the reactants' adsorption properties and intermediates.[18] Thus, the CeO_2–Pt alloy interfaces can facilitate the AOR.[13,19] However, CeO_2 generally possesses a low surface area (<50 m^2 g^{-1}), which is not sufficient for high-loading nanoparticle deposition and effective mass transfer. In contrast, the ZIF-8 derived carbon typically exhibits a large surface area and dominant porosity, ideal for Pt-based alloy nanoparticle deposition.[20–22]

Morphology characterization results have demonstrated that the ternary PtIrZn nanoparticles were uniformly deposited on the CeO_2-ZIF-8 support. To provide a more comprehensive understanding of these two different composite supports, we also used the SiO_2–CNT–COOH composite support for depositing PtIrZn nanoparticles. Both catalysts were further evaluated in DAFCs by using a high-performance anion-exchange membrane.[7,23] Electrochemical results displayed a similar intrinsic AOR activity (onset potential) on both CeO_2-ZIF-8 and SiO_2–CNT–COOH composite supports. The DAFC tests demonstrated that the PtIrZn/SiO_2–CNT–COOH could greatly enhance the electrical conductivity and mass transfer in the anode, yielding a remarkable power density of 314 mW cm^{-2}. We believe that the new knowledge for ammonia oxidation combined with the design and synthesis of advanced electrocatalyst alloys and supports in this work would advance the DAFC technology for possible transportation and other applications.

2. Results and discussion

2.1 Catalyst synthesis and characterization

A facile synthetic route for ternary PtIrZn nanoparticles (NPs) deposited on a binary composite support (*e.g.*, CeO_2/ZIF-8-derived carbon and SiO_2/CNT–COOH) was developed by reducing the metal precursors *via* sodium borohydride under an ultrasonic environment (Fig. 1). In the case of the CeO_2/ZIF-8 carbon support, diluted alkaline-treated CeO_2 acts as not only a support for metal NPs,[24] but also a reservoir for adsorbing OH species.[25] ZIF-8 derived carbon with unique micropores shows a large surface area ($\sim$600 m^2 g^{-1}, Fig. S1, ESI†),[18] and is an effective metal precursor (*i.e.*, $PtCl_4^{2-}$, $IrCl_6^{2-}$, and Zn^{2+}) for adsorption during synthesis. Also, the dominant N dopants in ZIF-8 derived-carbon provide sufficient defects to assist the dispersion of Pt-based nanoparticles due to

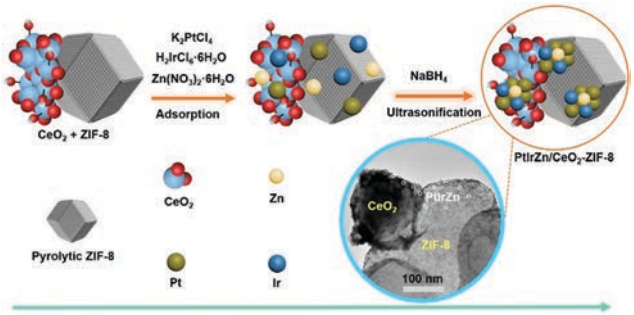

Fig. 1 Schematic illustration for the synthesis of CeO_2 and ZIF-8 supported ternary PtIrZn nanoparticles.

the electron-donation from nitrogen defects to Pt.[18,26,27] ZIF-8 derived carbon shows an average particle size of 200 ± 12.7 nm, as can be seen from the scanning electron microscopy (SEM) images (Fig. S2a and b, ESI†). Crystal structures of ZIF-8 precursors are converted into the carbon phase during a typically thermal activation process at 1100 °C for one hour under an Ar atmosphere, verified by analyzing their X-ray diffraction (XRD) patterns (Fig. S2c and d, ESI†).

During the synthesis, deionized water and ethanol were used to disperse the composite support and then adsorb the metal precursors in the support. Simultaneously, acoustic cavitation[28] was employed to control the nucleation and growth of PtIrZn ternary NPs with uniform size and distribution. Additionally, compared to platinum-group-metal (PGM) precursors ($PtCl_4^{2-}$ and $IrCl_6^{2-}$) for the PtIr/CeO_2-ZIF-8 (Fig. S3, ESI†), the smaller Zn^{2+} is easily adsorbed onto the pyrolytic ZIF-8 carbon support and interacts with the PGM ones. In doing so, the uniformly dispersed ternary PtIrZn alloy NPs were uniformly dispersed on the composite support consisting of CeO_2 (~100 ± 8.9 nm) and ZIF-8 derived carbon (Fig. S4, ESI†). The PGM (Pt or Pt–Ir) loadings for all the synthesized catalysts are 10 wt% *vs.* the support unless otherwise noted. Molar ratios of Pt : Ir : Zn in the PtIrZn/CeO_2-ZIF-8 are varied at 1 : 1 : 0.2 ($PtIrZn_1$), 1 : 1 : 0.6 ($PtIrZn_2$), and 1 : 1 : 1 ($PtIrZn_3$). Other control samples, such as PtIr/CeO_2-ZIF-8 and PtZn/CeO_2-ZIF-8 in a molar ratio of Pt : Ir and Pt : Zn = 1 : 1, as well as $PtIrNi_2$/CeO_2-ZIF-8 and $PtIrCu_2$/CeO_2-ZIF-8 in a molar ratio of Pt : Ir : Ni and Pt : Ir : Cu = 1 : 1 : 0.6, were synthesized *via* an identical procedure and the corresponding metal precursors.

Transmission electron microscopy (TEM) images show that the PtIr NPs have an average size of 7.1 ± 0.3 nm (Fig. S3c and d, ESI†). An interplanar spacing of 0.225 nm measured with these PtIr NPs in Fig. S5a and c (ESI†) suggests a lattice contraction compared to that of the pure Pt (*ca.* 0.227 nm).[29] Typically, PtIr alloys have a lattice parameter of *ca.* 2.25 Å in the (111) plane (Fig. S5b and d, ESI†), which agrees with the PtIr NPs on the composite support.[30] The electron diffraction (ED) pattern in Fig. S5f (ESI†) shows that the indices (*e.g.*, 111 and 200) are in good agreement with the face-centered cubic (fcc) lattice of PtIr NPs.[31] The high angle annular dark-field (HAADF) scanning transmission electron microscopy (STEM) and the corresponding elemental maps show that the Pt and Ir atoms are well dispersed throughout the PtIr NPs on the composite support (Fig. S5g, ESI†).

Unlike the PtIr/CeO_2-ZIF-8 sample, a more uniform Pt alloy NP dispersion is found for $PtIrZn_2$/CeO_2-ZIF-8 (Fig. 2a–c and Fig. S6, ESI†). This is likely due to it being much easier for the ZIF-8 derived carbon and OH^- abundant CeO_2 to trap the smaller Zn^{2+} that could assist the adsorption and distribution of Pt and Ir precursors (*i.e.*, $PtCl_4^{2-}$ and $IrCl_6^{2-}$) *via* electrostatic effects.[32–34] The diameter of the PtIrZn NPs was estimated to be 2.3 ± 0.2 nm, smaller than that of commercial PtIr/C (Fig. S7, ESI,† PtIr particle size: 2.7 ± 0.3 nm). The strong metal–support interactions between PtIrZn and the CeO_2 support (Fig. 2b) could be due to the semiconductor properties of CeO_2 for reducing PtIrZn alloy NPs.[24] The unique PtIrZn/CeO_2 interfaces could strengthen the interactions for metal-to-oxide and metal-to-metal bonds, thus restraining phase separation.[18,24] The lattice spacing of d = 0.312 nm is consistent with the (111) plane of fluorite-phase CeO_2 (Fig. 2b).[18,35] Different from the PtIrZn NPs deposited on the CeO_2 support, a higher loading of PtIrZn is observed on the ZIF-8 derived carbon support (Fig. 2c), which can be attributed to its high surface area (~600 $m^2\ g^{-1}$) and porosity. The HR-TEM image (Fig. 2d) and FFT pattern (Fig. 2e) display the interplanar spacing of 0.223 nm corresponding to d_{111} of fcc-PtIrZn alloy, illuminating a lattice contraction that occurs in PtIrZn NPs in contrast with that of the

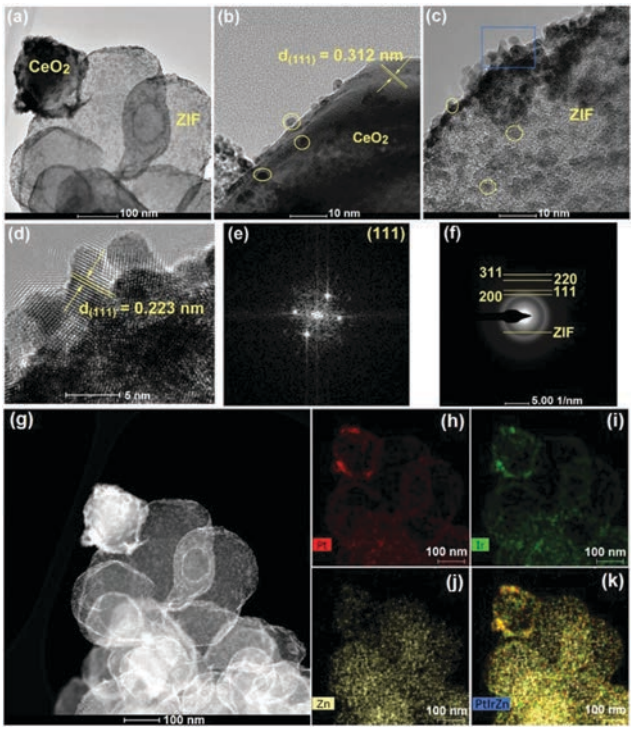

Fig. 2 Morphology, structure, and composition of the $PtIrZn_2$/CeO_2-ZIF-8 catalyst (molar ratio of Pt/Ir/Zn = 1 : 1 : 0.6). (a) TEM images, (b and c) HR-TEM images, (d) the enlarged area selected from (c), and (e) the FFT patterns of the corresponding nanoparticle in (d). (f) ED pattern from the selected area in (c). (g) HAAD-STEM image of (a), the corresponding EDS elemental mappings of Pt (h), Ir (i) and Zn (j), and the integrated mapping of Pt, Ir, and Zn (k).

PtIr NPs (*ca.* 0.225 nm) from commercial PtIr/C (Fig. S7, ESI†) and PtIr/CeO_2-ZIF-8 (Fig. S5, ESI†). The ED pattern in Fig. 2f shows that the indices (*e.g.*, 002, 111, and 200) are in accordance with the ZIF-8 derived carbon and fcc lattice of PtIrZn NPs. Also, the uniformly distributed PtIrZn NPs on the composite support can be further confirmed by the elemental mappings using energy-dispersive X-ray spectroscopy (Fig. 2(g–k)). Some Zn atoms can also be observed in the carbon support due to the incomplete thermal removal of Zn from the ZIF-8-derived carbon.[36]

X-ray diffraction (XRD) patterns were used to identify the crystal structure of these prepared catalysts. As shown in Fig. S8a (ESI†), the peak at ~26° of the Pt/ZIF-8 sample is attributed to the C (002) of the ZIF-8 derived carbon.[37] Other diffraction peaks at 2θ = 39.6, 47.4, 67.1, 81.2 and 83.6° correspond to the Miller indices of (111), (200), (220), (311) and (222) of fcc Pt for all the prepared Pt-based catalysts (Fig. S8, ESI†).[26] XRD peaks at 28.6°, 33.1°, 47.5°, 56.3°, 59.1°, 69.4°, 79.1°, and 88.4° in the CeO_2-involved catalysts can be ascribed to the Miller indices (111), (200), (220), (311), (222), (400), (331), and (420) of the cubic lattice of CeO_2 (JCPDS No. 81-0792, fluorite structural type), respectively (Fig. 3a and Fig. S8, S9, ESI†).[19]

After introducing Ir, Zn, and IrZn into the Pt base, XRD patterns verify the bimetallic PtIr and PtZn and ternary PtIrZn alloys with the face-centered cubic (fcc) crystal structure (Fig. 3a, b and Fig. S9, ESI†). Furthermore, fcc Pt peaks in these alloys shift toward higher angles, suggesting a reduced *d* space due to the alloying. Precisely, the *d* spaces in $PtIrZn_1$, $PtIrZn_2$, and $PtIrZn_3$ were calculated to be 0.2237, 0.2226, and 0.2223 nm, respectively, smaller than that of PtIr alloys (0.2252 nm). The contraction can be explained by the replacement of Pt by the smaller Ir and Zn atoms, leading to the decreased lattice spacing. Raman spectra (Fig. S10a, ESI†) have shown the identical D and G bands of the ZIF-8 derived carbon, as well as the CeO_2 peak.

X-ray photoelectron spectroscopy (XPS) results for several Pt-based catalysts (Fig. 3c and Fig. S10–S13, ESI†) are summarized in Table S1 (ESI†) concerning their chemical states and surface species. The atomic concentrations of Pt and Ir in the $PtIrZn_2$/CeO_2-ZIF-8 are determined to be 9.2 at% and 7.3 at%, respectively, which are higher than other catalysts, suggesting a stronger interaction between the binary support and Pt alloys.

In addition to pyridinic-, graphitic-, and oxidized-N,[38,39] the N 1s XPS peak at 399.7 eV could be ascribed to N species bonded to M sites,[40–42] likely Pt–N or Ir–N in the catalyst (Fig. S11, ESI†). The existence of pyridinic N can act as anchor sites for Pt and Ir atoms,[26,40] thereby increasing the average binding energy of N 1s. In Fig. 3c, the high-resolution Pt 4f spectra of all tested samples except for the $PtIrZn_2$/CeO_2-ZIF-8 can be deconvoluted into two doublets assigned to metallic Pt^0 and oxidized Pt(II).[41] Differently, two peaks with binding energies of 71.34 and 74.70 eV are observed in the Pt 4f XPS spectrum of $PtIrZn_2$/CeO_2-ZIF-8, indicating the dominant metallic Pt species. Introducing metals (*e.g.*, Ir and Zn) with smaller electronegativity into Pt could result in a negative shift of binding energies for Pt in its alloys,[19] as can be

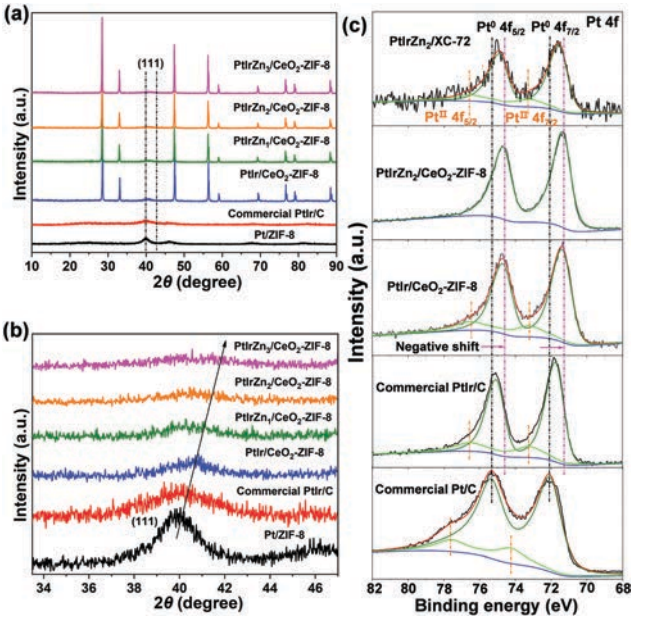

Fig. 3 XRD patterns of (a) Pt/ZIF-8, commercial PtIr/C, PtIr/CeO_2-ZIF-8, $PtIrZn_1$/CeO_2-ZIF-8, $PtIrZn_2$/CeO_2-ZIF-8, and $PtIrZn_3$/CeO_2-ZIF-8, and (b) the corresponding enlarged region from 33° to 47° for these Pt-based catalysts. (c) High-resolution Pt 4f XPS spectra of various Pt-based catalysts.

demonstrated by the binding energy shifts of Pt $4f_{5/2}$ (0.24 and 0.42 eV) and Pt $4f_{7/2}$ (0.30 and 0.48 eV) for the PtIr/C and $PtIrZn_2$/XC-72, respectively, when compared to the Pt/C catalyst (Table S2, ESI†). It should be noticed that the binding energy shifts of Pt $4f_{5/2}$ (0.60 eV) and Pt $4f_{7/2}$ (0.70 eV) for the PtIr/CeO_2-ZIF-8 are significantly larger than those of the PtIr/C catalyst, indicating the intense electron interactions between Pt and the CeO_2 support, as well as the coordinated N, which would be beneficial for electrocatalytic properties.[20,38]

2.2 Catalyst activity for the AOR

The AOR activity of all catalysts was assessed using a rotating disk electrode (RDE) in 1.0 M KOH + 0.1 M NH_3 electrolyte. The synergy between CeO_2 and ZIF-8 was confirmed by a noticeable AOR activity enhancement when Pt nanoparticles were deposited on various supports (Fig. S14a, ESI†). In alkaline electrolytes, CeO_2 is a reservoir for OH adsorption. The adsorbed OH groups at the catalyst surface could participate in the AOR,[17,25] leading to an enhanced AOR activity. Several commonly used carbon materials, including carbon black (XC-72), carboxyl-functionalized CNTs (CNT–COOH), and ZIF-8 derived carbon, were integrated with CeO_2 for Pt nanoparticle deposition as AOR catalysts. The electrochemical impedance spectroscopy (EIS) results (Fig. S14b, ESI†) demonstrate that these studied supports display different charge transfer resistance. Overall, the CNT-containing support presents the smallest resistance, while the ZIF-8 carbon based support shows the largest resistance, which is likely due to their electrical conductivity. However, the ZIF-8 carbon displayed the highest AOR activity (Fig. S14a, ESI†). This is because of its large surface area

(Fig. S1, ESI†) and sufficient defects in the ZIF-8-derived carbon benefitting the uniform dispersion of Pt nanoparticles. Additionally, the optimization of the carbon content in the composite support was investigated, and it was found that 33.3 wt% ZIF-8 derived carbon in the support led to the highest AOR activity (Fig. S14c, ESI†). This composition was then used for all further experiments. The chronoamperogram (CA) results, *i.e.*, *i–t* curves (Fig. S15, ESI†), of all Pt catalysts, are consistent with their corresponding AOR activity determined by cyclic voltammetry (CV) using a sufficiently low scanning rate. Accordingly, the best-performing composite support of CeO_2 and ZIF-8 was used for further studies.

To enhance the catalytic activity of Pt catalysts, either Ir or Zn was alloyed with Pt at a molar ratio of 1 : 1. The improved AOR activities of both PtIr/CeO_2-ZIF-8 and PtZn/CeO_2-ZIF-8 were demonstrated in terms of the increased current density at 0.5 V *vs.* RHE (Fig. 4a, b and Table S3, ESI†).[13,43] A dramatically reduced onset potential (0.417 V *vs.* RHE) for PtIr/CeO_2-ZIF-8 compared to that of Pt/CeO_2-ZIF-8 (0.504 V) is attributed to favorable NH_3 adsorption and dehydrogenation.[44,45] Also, a reduced onset potential (0.468 V) for PtZn/CeO_2-ZIF-8 is likely because alloying Zn could inhibit the competitive hydrogen adsorption.[46,47] Furthermore, Ir and Zn were then simultaneously alloyed with Pt to prepare a ternary catalyst. Compared to the binary PtIr/CeO_2-ZIF-8 (peak current density, J_p: 15.7 A g^{-1}, onset potential, E_{onset}: 0.417 V) and PtZn/CeO_2-ZIF-8 catalysts (19.9 A g^{-1} and 0.468 V), the PtIrZn_2/CeO_2-ZIF-8 catalyst demonstrated a significantly improved AOR activity (Fig. 4a) in terms of both the increased J_p (31.8 A g^{-1}) and the reduced E_{onset} (0.345 V). The AOR activity is significantly superior to that of the commercial PtIr/C catalyst (25.1 A g^{-1} and 0.428 V). Note that the PGM loading is used to quantify the current for all studied catalysts.

Zn has a high overpotential for hydrogen evolution.[15] Therefore, the introduction of Zn into Pt or PtIr could suppress the hydrogen adsorption, as evidenced in the CV curves recorded in Ar-saturated 0.1 M KOH solutions for various catalysts, including Pt/CeO_2-ZIF-8, PtIr/CeO_2-ZIF-8, PtZn/CeO_2-ZIF-8, and PtIrZn_2/CeO_2-ZIF-8 (Fig. S16, ESI†). The hydrogen adsorption/desorption occurs over 0 to 0.40 V *vs.* RHE, where the adsorption of ammonia would compete against the hydrogen adsorption. The addition of Zn might inhibit the competitive hydrogen adsorption (Table S4, ESI†), leading to a decrease in onset potentials for the AOR (Fig. 4a).

In general, the amount of introduced third metal (*e.g.*, Zn or Ni[13]) in the ternary alloys will result in effects on their electronic structure, therefore affecting NH_3 adsorption and N–H

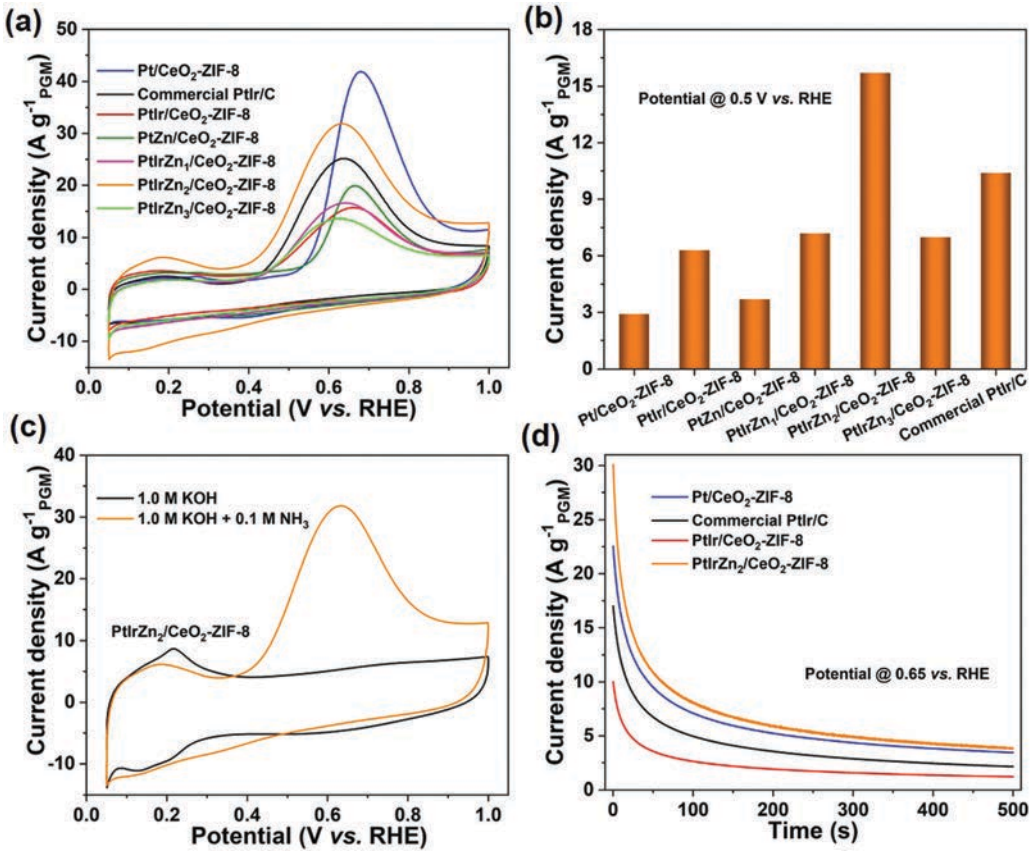

Fig. 4 CV curves for different catalysts in Ar-saturated 1.0 M KOH + 0.1 M NH_3 at 5 mV s^{-1} and 900 rpm under ambient conditions: (a) comparison between Pt, PtIr, PtZn, PtIrZn_1, PtIrZn_2, PtIrZn_3 deposited on the CeO_2-ZIF-8 support and the commercial PtIr/C catalyst. (b) AOR activity comparison for various catalysts in (a) at 0.5 V *vs.* RHE. (c) CV curves of the PtIrZn_2/CeO_2-ZIF-8 catalyst in the presence and absence of NH_3. (d) Chronoamperograms (CA) of the Pt/CeO_2-ZIF-8, commercial PtIr/C, PtIr/CeO_2-ZIF-8, and PtIrZn_2/CeO_2-ZIF-8 in Ar-saturated 1.0 M KOH with 0.1 M NH_3 at 900 rpm at 0.65 V *vs.* RHE under ambient conditions.

bond activation differently. Although the $PtIrZn_2/CeO_2$-ZIF-8 catalyst performs the best, other studied Zn contents in PtIrZn catalysts (*e.g.*, $PtIrZn_1/CeO_2$-ZIF-8 and $PtIrZn_3/CeO_2$-ZIF-8) do not exhibit enhanced activity compared to the Pt/CeO_2-ZIF-8 catalyst (Fig. 4a, b and Table S3, ESI†). Because only Pt or Ir sites can adsorb NH_3 for subsequent dehydrogenation at room temperature, energy factors relating to bond cleavage and geometric factors are sensitive to the Zn content. An appropriate amount of Zn added into the PtIr system is needed to maintain Pt–Ir sites' density for N–H bond activation and breaking. Considering both the J_p and the E_{onset} (Table S3, ESI†), the $PtIrZn_2/CeO_2$-ZIF-8 (molar ratio of Pt/Ir/Zn = 1 : 1 : 0.6) was regarded as the optimal ternary PtIrZn AOR catalyst, which was further studied in the next sections.

The synergy between CeO_2 and ZIF-8 was further confirmed by the enhanced AOR activity of $PtIrZn_2$ nanoparticles supported on CeO_2-ZIF-8 (current density: 15.7 A g^{-1} at 0.5 V) when compared to the individual CeO_2 (current density: 3.6 A g^{-1} at 0.5 V), and ZIF-8-derived carbon (current density: 10.9 A g^{-1} at 0.5 V *vs.* RHE) supports (Table S5, ESI†). The higher AOR activity of the $PtIrZn_2/CeO_2$-ZIF-8 catalyst is attributed to fast scavenging of the *NH species adsorbed on Pt alloy sites by reaction with OH adsorbed on adjacent CeO_2 sites at lower oxidation potential.[13,25] More significantly, the optimal PtIrZn catalyst supported on the CeO_2-ZIF-8 binary support shows much better AOR activity relative to the commercial XC-72 support (Fig. S16 and S17, ESI†). Thus, the interfaces between the active metal sites (*i.e.*, PtIrZn) and advanced support (*i.e.*, CeO_2-ZIF-8) are the critical factors for the enhanced AOR activity. Likewise, another composite support consisting of SiO_2–CNT–COOH yields enhanced AOR activity.[13] The PtIrZn nanoparticles (*e.g.*, Fig. 2b) directly attached to the CeO_2 may have enhanced intrinsic AOR activity because the supplied OH groups from CeO_2 readily accept a proton and facilitate the critical NH_3 dehydrogenation (*e.g.*, $NH_{3,ad} + OH^- \rightarrow NH_{2,ad} + H_2O + e^-$). Meanwhile, the ZIF-8-derived carbon typically exhibits a large surface area and porosity, maximizing the Pt alloy utilization and enriching CeO_2 and PtIrZn NP interfaces.

Fig. 4c presents typical CV curves for the optimal PtIrZn catalyst in 0.1 M KOH in the presence and absence of NH_3, showing an NH_3 oxidation peak in the potential range of 0.30–0.95 V. A small pre-peak at around 0.22 V before the AOR peak is likely attributed to the chemical adsorption of NH_3.[48,49] The deactivation at higher potential ranges (0.64–0.92 V) is due to the strongly adsorbed reaction intermediates (*e.g.*, *N and *NO) that block the active Pt alloy surface.[13,43] CA results (Fig. 4d and Fig. S17, ESI†) further determine that the optimal PtIrZn catalyst has the highest current density (*e.g.*, 3.9 A g^{-1} after 500 s) at 0.65 V, superior to Pt/CeO_2-ZIF-8 (1.2 A g^{-1}) and commercial Pt/C (2.2 A g^{-1}) catalysts. It should be pointed out that these CAs show a rapid drop of the current until attaining a steady-state. At the beginning of the reaction, the active sites (*i.e.*, Pt or PtIr) are likely free for adsorbing NH_3 molecules. The initial activity drop is due to the reduction of Pt site density caused by the poisoning with *N or *NO_x species as the reaction proceeds.[13,50]

To further determine the superiority of ternary PtIrZn, the most studied Ni and Cu were selected as the third metals alloying with PtIr. As discussed above, Zn's optimal addition into PtIr can suppress the hydrogen adsorption, playing a critical role to facilitate the AOR (Fig. S16 and Table S4, ESI†). In contrast, Ni and Cu's addition to PtIr affects the hydrogen adsorption–desorption behaviors differently (Fig. S18a, ESI†). As a result, the AOR activity for these three ternary alloys is in the order of PtIrZn > PtIrNi > PtIrCu, with the corresponding onset potentials of 0.345, 0.414, and 0.418 V (Fig. S18b and Table S5, ESI†). This activity order was further demonstrated by their current densities (*i.e.*, 15.7, 7.7, and 6.3 A g^{-1}) at 0.5 V (Fig. S18c, ESI†) from CVs and their corresponding CA results (Fig. S18d, ESI†).

Overall, the AOR activity of the best-performing $PtIrZn_2/CeO_2$-ZIF-8 catalyst (molar ratio of Pt/Ir = 1 : 1, E_{onset}: 0.345 V *vs.* RHE, J_p: 31.8 A g^{-1}) is superior or comparable to those of many reported catalysts, such as PtZn nanocubes/C catalyst (E_{onset}: ~0.5 V *vs.* RHE, J_p: 405 A g^{-1}),[46] PtIr/N-reduced graphene oxide (rGO) (molar ratio of Pt/Ir = 1 : 3, E_{onset}: ~0.37 V *vs.* RHE),[51] PtIrNi/SiO_2–CNT–COOH (molar ratio of Pt/Ir = 9 : 1, E_{onset}: ~0.399 V *vs.* RHE, J_p: 124.0 A g^{-1}),[13] PtIrNi/CeO_2–CNT–COOH (molar ratio of Pt/Ir = 9 : 1, E_{onset}: ~0.465 V *vs.* RHE, J_p: 34.0 A g^{-1}),[13] CuPtRh nanowires (mass ratio of Pt/Ru = 7 : 1, E_{onset}: ~0.49 V),[52] and Ir and $Ni(OH)_2$-decorated Pt nanocubes (mass ratio of Pt/Ir = 98 : 2, E_{onset}: ~0.51 V).[50] Detailed comparisons of the aforementioned AOR catalysts in terms of E_{onset} and/or J_p are provided in Table S5 (ESI†).

The $PtIrZn_2/CeO_2$-ZIF-8 catalyst also shows good stability for the AOR. Continuous CV cycling over the potential range of 0.05–0.7 V at 500 mV s^{-1} was conducted in Ar-saturated 1.0 M KOH solutions to evaluate the catalyst's degradation. After 2000 cycles, the Pt/C benchmark rapidly lost 65% of its initial electrochemically active surface area (ECSA).[13] In contrast, the $PtIrZn_2/CeO_2$-ZIF-8 catalyst exhibited much better cycling stability, retaining more than ~85% of the initial ECSA (Fig. S19a, ESI†). The ECSA reduction of these two catalysts is in good agreement with their AOR activity losses (Fig. S19a, ESI†). The $PtIrZn_2/CeO_2$-ZIF-8 catalyst showed only a 32 mV positive shift of peak potential and a loss of ~3.0% peak current density, whereas the Pt/C benchmark displayed ~46 mV positive shift of peak potential and a loss of 51% peak current density.[13] Therefore, both the chronoamperometric durability (Fig. 4d) and the cycling stability (Fig. S19, ESI†) of $PtIrZn_2/CeO_2$-ZIF-8 have exceeded the Pt/C catalyst.

2.3 Critical factors of AOR rates

In addition to the catalyst, AOR can be affected by critical reaction conditions, such as the operating temperature, NH_3 concentration, and KOH concentration.[43,53] The effect of operating temperature was investigated on the best-performing $PtIrZn_2/CeO_2$-ZIF-8 catalyst and the commercial Pt/C reference (Fig. 5a). The oxidation peak current densities of both catalysts rise rapidly with the temperature elevating up to 80 °C, attributable to the improved kinetics of NH_3 oxidation.[53] Strikingly, the AOR onset potential of the PtIrZn catalyst shifts from

0.33 V at 25 °C to 0.25 V at 80 °C, and its J_p increases from 38 to 418 A g^{-1}. The CV curves (Fig. 5a) also exhibit a 102 mV negative shift of the peak potential from 25 to 80 °C. With an increase of temperature, the *N intermediate can form less positive potential, allowing a higher reaction rate at a lower overpotential.[13] The N–N dimerization reactions become more accessible at higher temperatures.[43,44] Steady-state CA results of the $PtIrZn_2/CeO_2$-ZIF-8 (Fig. S20a, ESI†) at different temperatures are consistent with its CV results, further confirming the advantage of the elevated temperatures for the AOR. Fig. 6b shows the Arrhenius plots for the $PtIrZn_2/CeO_2$-ZIF-8 and the commercial PtIr/C catalysts at 0.5 V. Good linear relationships are achieved by plotting log(J) and $1/T$, indicating that the reaction mechanism is not changed with increasing temperature.[53] According to the Arrhenius law, their activation energy can be calculated using the equation.[53,54] The activation energies at 0.5 V were calculated to be 36.7 and 50.8 kJ mol^{-1} for the $PtIrZn_2/CeO_2$-ZIF-8 and commercial PtIr/C catalysts, respectively (Fig. 5b). The lower activation energy of the PtIrZn catalyst unveils its higher intrinsic activity, faster charge transfer process, and less energy-consumption in the reaction.[53]

AOR activity of the $PtIrZn_2/CeO_2$-ZIF-8 catalyst is increased with the NH_3 concentration (Fig. 5c). The current density was increased from 9.4 to 17.6 A g^{-1} when the concentrations of NH_3 are from 0.05 to 1.0 M at 0.5 V (Fig. 5d). Higher NH_3 concentrations lead to faster current attenuation (Fig. S20b, ESI†), which can be attested by a lower remaining current density at 1.0 M NH_3 (4.8 A g^{-1}) than 0.5 M NH_3 (5.1 A g^{-1}) after 500 s. These results indicate that more poisonous adsorbates could be accumulated in an electrolyte with a higher NH_3 concentration during the AOR.

Given a constant NH_3 concentration and under room temperature, the OH^- concentration in the electrolytes can substantially influence the AOR rates. Fig. 5d and Fig. S20c (ESI†). CA tests show the effect of KOH concentration on the AOR activity of the $PtIrZn_2/CeO_2$-ZIF-8 catalyst. Higher OH^- concentration can lower the AOR onset potential. It also increases the peak current density (Fig. 5e). When the OH^- concentrations are increased from 1.0 to 5.0 M, the onset potentials are reduced from 0.345 to 0.314 V, and the peak current densities are increased from 31.8 to 65.1 A g^{-1}. The improved AOR activity at higher OH^- concentration is likely due to smaller charge transfer resistance (R_{ct} = 16.6, 19.8, and 60.4 Ω for 5.0, 3.0, and 1.0 M KOH, respectively, Fig. 5f).[7,55]

2.4 Theoretical studies of the AOR

To understand Zn's role in the ternary PtIrZn catalyst for the AOR, we performed DFT calculations for appropriate reaction steps on three models, including bimetallic Pt_2Ir_2 and Pt_2Ir_2 systems with a relatively low and medium Zn content (Pt_2Ir_2–Zn_{lc} and Pt_2Ir_2–Zn_{mc}). All models were simulated in the fcc phase. The (100)-termination was chosen because of its unique structure toward N–N coupling, a crucial step for ammonia oxidation.[56] Because of Zn's strong oxophility and the abundance of OH_{ad} from the CeO_2 support, the surface bridge sites are pre-covered with 1/4 ML *OH species. The limiting potential

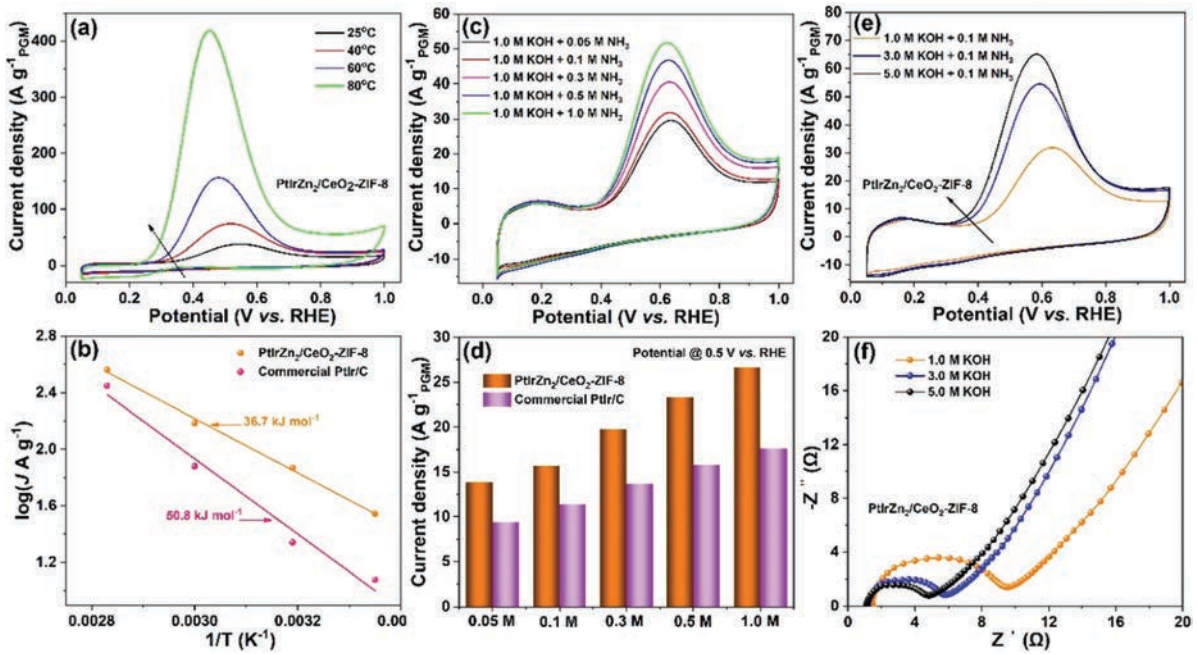

Fig. 5 (a) CV curves at 5 mV s^{-1} and 900 rpm for the $PtIrZn_2/CeO_2$-ZIF-8 catalyst in Ar-saturated 1.0 M KOH + 0.1 M NH_3 recorded at different temperatures. (b) Arrhenius plots for NH_3 oxidation on $PtIrZn_2/CeO_2$-ZIF-8 and commercial PtIr/C catalysts at 0.5 V *vs.* RHE. (c) CVs for the AOR in 1.0 M KOH electrolytes with different NH_3 concentrations atr room temperature. (d) AOR activity comparisons at 0.5 V *vs.* RHE for $PtIrZn_2/CeO_2$-ZIF-8 and commercial PtIr/C at different NH_3 concentrations. Note: the PtIr/C benchmark was compared according to our previous report.[13] (e) CVs for the AOR in various electrolytes containing 0.1 M NH_3 and different KOH concentrations at room temperature. (f) Nyquist plots of EIS spectra measured for the $PtIrZn_2/CeO_2$-ZIF-8 catalyst in different KOH concentrations at the open circuit potential.

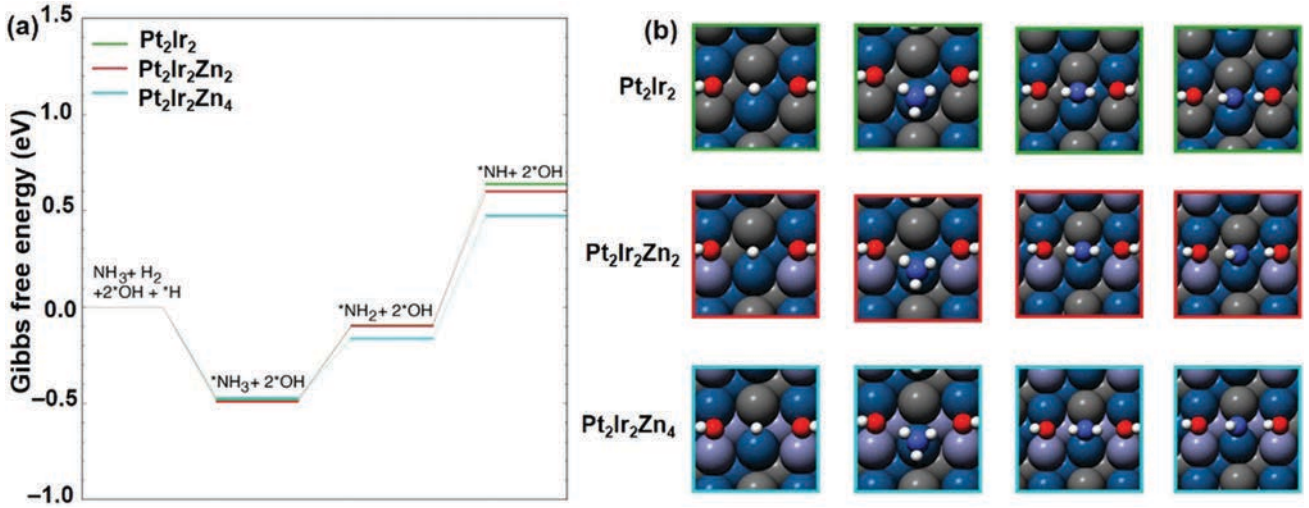

Fig. 6 (a) Free energy diagrams of NH_3 oxidation on Pt_2Ir_2 and its ternary alloy with Zn at 0 V *vs.* RHE. (b) Geometric structures of clean, $*NH_2$, and *NH intermediates on Pt_2Ir_2 and its alloys with Zn. (Grey: Pt, dark blue: Ir, purple: Zn, red: O, white: H, and blue: N).

of $*NH_2$ to *NH with the hydrogen bonding interaction with OH is a useful indicator for capturing the onset potential of the AOR on Pt(100) and its alloys.[13,56] *NH–*NH dimerization is the dominant pathway toward N_2 formation. Fig. 6 shows the free energy diagram of the initial steps of NH_3 oxidization at 0 V. Compared to the Pt–Ir bridge site on $Pt_2Ir_2(100)$, a low concentration of Zn (preferred at the surface because of strong interaction with *OH) stabilizes the $*NH_2$ and *NH intermediates only slightly with a reduction of the limiting potential <0.03 V. The Zn atom has a weaker d–d coupling to the Pt–Ir group d-orbitals, which will shift up the d-band and facilitate the hydrogenation of $*NH_2$ species. Fortunately, the sp-electron transfer from the electron-rich Zn atoms to the Pt–Ir site has an opposite effect. As the Zn concentration increases in the Pt_2Ir_2–Zn_{mc} model, the stabilization of *NH is 0.1 eV more than the $*NH_2$ species, which leads to a 0.1 V reduced onset potential of the PtIrZn catalyst as observed experimentally. We attributed this effect to Zn-induced electronic structure change as the average of the d-band center is increased from -0.7 eV in the Pt_2Ir_2 to -0.52 eV in the Pt_2Ir_2–Zn_{mc}. Another effect is the competitive adsorption between *H and $*NH_3$. At Pt(100), the adsorption/desorption of *H occurs at the potential of 0.2–0.4 V, which overlaps with the operating potential of AOR at $\sim$0.3 V. The strongly binding *H might block the active Pt–Ir site for the NH_3 adsorption. The free energy of $*NH_3$ adsorption at the Pt–Ir site is 0.6 eV stronger than Pt(100). Although Zn stabilizes both intermediates on PtIrZn catalysts, it becomes more favorable for *H removal with $*NH_3$ adsorption, resulting in a less positive potential of *H oxidation. This result is impressive since it is generally believed that Zn destabilizes the *H, prohibiting the HER. Our DFT calculations suggest that incorporating Zn into PtIr leads to a stronger $*NH_3$ adsorption than *H adsorption, which is kinetically favorable for the AOR.

2.5 Low-temperature direct ammonia fuel cell performance

The typical set-up for a DAFC is illustrated in Fig. 7a. NH_3 reacts with OH^- and is oxidized at the anode to provide electrons and generate N_2 ($2NH_3 + 6OH^- = N_2 + 6H_2O + 6e^-$, $E^0 = -0.77$ V *vs.* SHE). O_2 consumes electrons and generates OH^- ($O_2 + 2H_2O + 4e^- = 4OH^-$, $E^0 = 0.401$ V *vs.* SHE) at the cathode.[11] In theory, the overall reaction can generate a cell voltage up to 1.17 V, which is only slightly lower than an H_2–O_2 fuel cell.

Unlike in aqueous electrolytes, high-performance OH^--exchange membranes and ionomers developed at the University of Delaware were integrated with these studied PtIrZn catalysts for fabricating membrane electrode assemblies (MEAs) for DAFC studies.[7,57] The cathode is an Acta 4020 catalyst (*i.e.*, 3.5 wt% transition iron metal on carbon support) for the oxygen reduction reaction (ORR). During the DAFC studies, we selected four PtIr-based catalysts concerning the variations of supports (*i.e.*, CeO_2/ZIF-8-carbon, SiO_2/CNT–COOH, and commercial XC-72) and metal nanoparticles (*i.e.*, PtIr and $PtIrZn_2$, 1.0 mg_{PGM} cm^{-2}). RDE measurements (Fig. 7b) indicate that their AOR activities in an aqueous electrolyte (KOH + NH_3) follow the order: $PtIrZn_2/SiO_2$–CNT–COOH > PtIr/SiO_2–CNT–COOH > $PtIrZn_2/CeO_2$-ZIF-8 > commercial PtIr/C, as evidenced by their current densities of 32.4, 24.7, 15.7, and 10.4 A g^{-1} at 0.5 V, respectively.

The polarization curves of DAFCs at 95 °C by using different anode catalysts were recorded as shown in Fig. 7c. The open-circuit voltages (OCVs) with these studied $PtIrZn_2/CeO_2$-ZIF-8, PtIr/SiO_2–CNT–COOH, and $PtIrZn_2/SiO_2$–CNT–COOH anodes are 0.64, 0.70, and 0.70 V, respectively, comparable to that of the commercial PtIr/C (0.69 V). The MEA testing results show a different trend to their AOR onset potentials evaluated by RDE (Fig. 7b). A similar phenomenon was found on the peak power densities, showing 91 mW cm^{-2} for the $PtIrZn_2/CeO_2$-ZIF-8, 241 mW cm^{-2} for the PtIr/C, 282 mW cm^{-2} for the PtIr/SiO_2-CNT-COOH, and 314 mW cm^{-2} for the $PtIrZn_2/SiO_2$–CNT–COOH. From the high-frequency resistance (HFR) result recorded by the EIS module of the fuel cell test station, the HFR of MEA with the $PtIrZn_2/CeO_2$-ZIF-8 catalyst is 110 mΩ cm^{-2}, which is much larger than those of MEAs with $PtIrZn_2/SiO_2$–CNT–COOH and

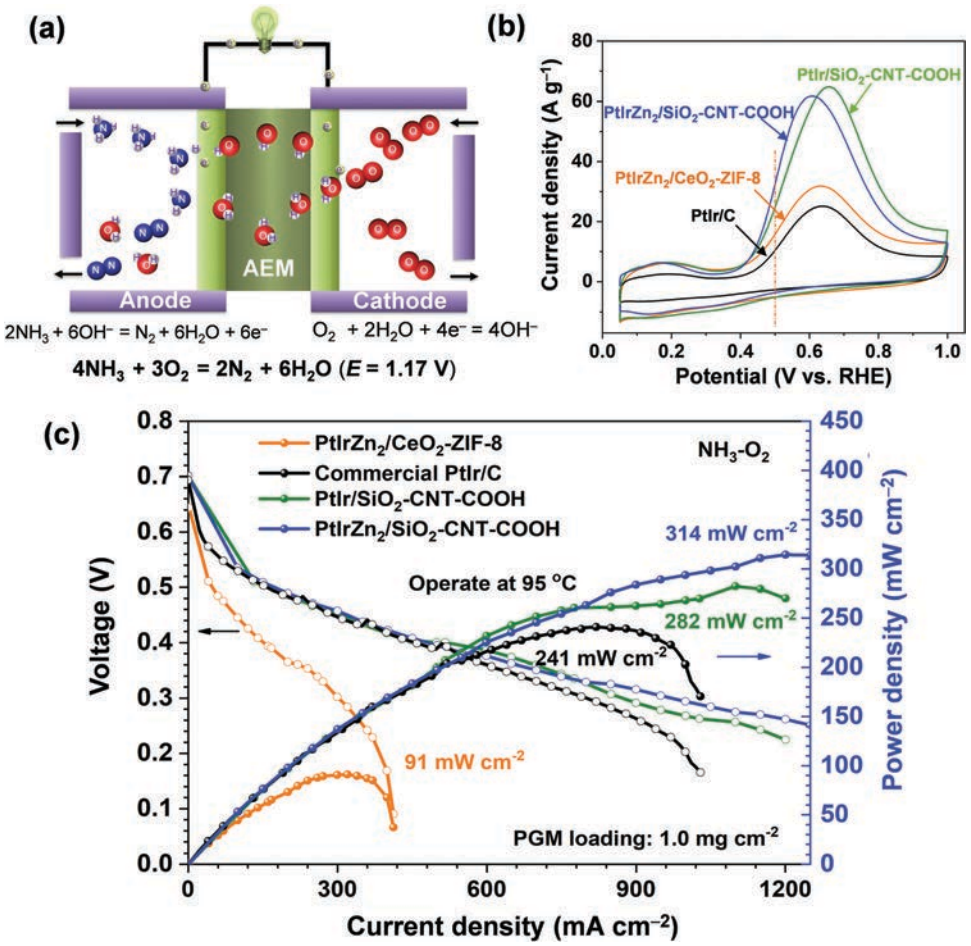

Fig. 7 (a) Schematic view of components and working principles of a DAFC. (b) AOR activity comparison of $PtIrZn_2/CeO_2$-ZIF-8 (Pt–Ir, 10 wt%), commercial PtIr/C (Pt–Ir, 40 wt%), $PtIr/SiO_2$–CNT–COOH (Pt–Ir, 10 wt%), and $PtIrZn_2/SiO_2$–CNT–COOH (Pt–Ir, 20 wt%) in 1.0 M KOH + 0.1 M NH_3 at 5 mV s^{-1} and 900 rpm under ambient conditions. (c) Polarization curves and power density curves of DAFCs with $PtIrZn_2/CeO_2$-ZIF-8, PtIr/C, $PtIr/SiO_2$–CNT–COOH, and $PtIrZn_2/SiO_2$–CNT–COOH anodes. The ORR cathode catalyst is a Fe-based commercial Acta 4020. The anode contains 1.0 mg_{PGM} cm^{-2} with 10 wt% PAP-TP (terphenyl-based) ionomer. The cathode contains 2.0 mg cm^{-2} of Acta 4020 with 20 wt% PAP-TP ionomer. The hydroxide exchange membrane (HEM) is PAP-TP (81 μm thickness). Testing conditions: cell temperature of 95 °C, 7.0 M NH_3 in 1.25 M KOH aqueous solution (5.0 mL min^{-1}) at 1.0 bar backpressure; O_2 (500 mL min^{-1}) at 2.0 bar backpressures.

$PtIr/SiO_2$–CNT–COOH, which are 65 mΩ cm^{-2} for both. The HFR of MEA with commercial PtIr/C is 50 mΩ cm^{-2}. The resistance comparison of MEAs is inconsistent with Nyquist plots recorded by using RDE (Fig. S21, ESI†).

Nevertheless, the improved cell performance of the $PtIrZn_2/SiO_2$–CNT–COOH relative to the $PtIr/SiO_2$–CNT–COOH further determines the significance of introducing Zn into PtIr alloys. The higher power density of DAFCs with the catalysts supported on the SiO_2/CNT–COOH support also justifies the critical role of the supports in boosting charge and mass transport within electrodes (Fig. 7c). The relatively poor DAFC performance with the $PtIrZn_2/CeO_2$-ZIF-8 anode may be due to the high resistance caused by non-uniform ionomer distribution and less efficient mass transport caused by dominant micropores in the ZIF-8-derived carbon. In contrast, the SiO_2–CNT–COOH composite support can provide more efficient charge and mass transport, which is critical for enhanced MEA performance.[58]

Compared to previous DAFC performance in the literature, the $PtIrZn_2/SiO_2$–CNT–COOH anode has the best performance (Table S6, ESI†). Notably, given the significant activity difference between the PtIrZn/SiO_2–CNT–COOH and the commercial PtIr/C (Fig. 7b), we should expect further improved DAFC performance with continuously studying MEA design and fabrication. It should be noted that, apart from intrinsic activity, the catalyst morphology and structures are essential for MEA performance. It is often challenging to directly transfer high RDE activity in aqueous electrolytes to solid-state electrolyte-based MEA performance because of the complicated triple-phase interfaces for charge and mass transports in thick and porous electrodes.[59] Based on the obtained knowledge on H_2–O_2 and direct methanol fuel cells,[60–62] DAFC performance can be improved by increasing the PGM loading on the supports, optimizing the interaction between PtIrZn alloy NPs and the support, engineering the interfaces of the catalyst and the ionomer for OH^- transfer within the electrode, and improving electrode structures with better ammonia permeability.[7,9,63]

3. Conclusions

In summary, inspired by theoretical understanding, we designed and synthesized PtIrZn ternary alloy catalysts supported on various composite supports for the AOR in DAFCs. In particular, well-defined PtIrZn alloy nanoparticles can be uniformly dispersed on a composite support consisting of CeO_2, and ZIF-8 derived carbon, with an average diameter of 2.3 ± 0.2 nm. In principle, CeO_2 can serve as a Lewis base and provide OH for facilitating the AOR. The high surface area, dominant porosity, and N dopant in the ZIF-8-derived carbon can be favorable for generating fine alloy nanoparticles during the synthesis. The combination of CeO_2 and ZIF-8 carbon can enrich the CeO_2–Pt alloy interfaces, thus enhancing the AOR activity. Similarly, we further employed the SiO_2–CNT–COOH composite support for preparing the ternary PtIrZn catalyst. Unlike CeO_2, SiO_2 possesses a high surface area and plays a similar role in facilitating the AOR by providing OH groups. It should be noted that the combination of CeO_2 and CNTs was explored as well, but both have low surface areas and cannot achieve uniform metal NP dispersion.

RDE results indicate that the optimal PtIrZn catalyst at a molar ratio of 1 : 1 : 0.6 shows superior AOR activity and stability in alkaline media relative to the commercial PtIr/C. DFT calculations suggest that Zn atoms' addition into the PtIr alloy modulates the electronic structure of Pt–Ir active ensembles on the (100) surface for facilitating dehydrogenation steps of adsorbed NH_3. Similar to Zn's role in enhancing AOR activity, Ni or Cu were also introduced into the PtIr baseline. Their AOR activities are in the order of PtIrZn > PtIrNi > PtIrCu. The kinetics of AOR is strongly dependent on the operation temperature, NH_3 concentration, and KOH concentration in aqueous electrolytes. The increasing temperature results in a significantly increased current density and reduced overpotentials. The AOR activity is also enhanced with NH_3 concentration, but a higher concentration of NH_3 may accelerate the catalyst deactivation. Higher OH^- concentration lowers the AOR onset potential and increases the peak current density, likely due to the fast AOR kinetics and smaller charge transfer resistances.

Multiple studied PtIrZn catalysts and the commercial PtIr/C were further evaluated in DAFCs by using OH^- exchange membranes and ionomers. At first, the $PtIrZn_2/CeO_2$-ZIF-8 (Pt–Ir, 10 wt%) anode catalyst does not present encouraging DAFC performance and only exhibited a moderate peak power density of 91 mW cm^{-2} due to a large charge transfer resistance and low mass transport. When PtIrZn alloy NPs were deposited on an alternative composite support consisting of high-surface-area SiO_2 and highly electrically conductive CNT–COOH, the PtIrZn/SiO_2–CNT–COOH anode catalyst achieved a compelling peak power density of 314 mW cm^{-2}, much higher than PtIr/SiO_2-CNT-COOH (282 mW cm^{-2}) and PtIr/C (241 mW cm^{-2}) controls. The enhanced DAFC performance further justifies the importance of innovative supports and PtIrZn catalysts for the AOR in actual MEAs. Further engineering electrode structures and MEA fabrication concerning advanced catalyst and support designs, catalyst/ionomer interfaces, and porosity for NH_3 permeability could dramatically improve DAFC performance for promising transportation and other applications.

Author contribution

G. W., Y. Y., H. X., J. Y., and Y. L. proposed the concept and designed all of the experimental and theoretical studies. Y. L., Z. Q., and M. C. carried out materials synthesis and characterization. H. S. P. and Q. M. performed DFT calculations. S. H. and D. S. conducted electron microscopy studies. S. K. analyzed XPS data. T. W. and Y. Z. tested the fuel cell performance. G. W., Y. Y., H. X., and Y. L. wrote the manuscript.

Conflicts of interest

There are no conflicts to declare.

Acknowledgements

This work was financially supported by start-up funding from the University at Buffalo, SUNY along with the U.S. Department of Energy's Advanced Research Projects Agency-Energy (ARPA-E) office's REFUL program. Electron microscopy research was conducted at the Center for Functional Nanomaterials at Brookhaven National Laboratory under Contract DE-SC0012704, which is DOE Office of Science User Facilities. J. Yang thanks the support from the National Natural Science Foundation of China (Grant No. 51972150). Y. Li is thankful for the support from China Scholarship Council (201808320253).

Notes and references

1 Y. Li, H. Wang, C. Priest, S. Li, P. Xu and G. Wu, *Adv. Mater.*, 2021, **33**, 2000381.
2 Y. Zhu, J. Sokolowski, X. Song, Y. He, Y. Mei and G. Wu, *Adv. Energy Mater.*, 2020, **10**, 1902844.
3 D. R. MacFarlane, P. V. Cherepanov, J. Choi, B. H. R. Suryanto, R. Y. Hodgetts, J. M. Bakker, F. M. Ferrero Vallana and A. N. Simonov, *Joule*, 2020, **4**, 1–20.
4 S. Mukherjee, S. V. Devaguptapu, A. Sviripa, C. R. F. Lund and G. Wu, *Appl. Catal., B*, 2018, **226**, 162–181.
5 S. Mukherjee, X. Yang, W. Shan, W. Samarakoon, S. Karakalos, D. A. Cullen, K. More, M. Wang, Z. Feng, G. Wang and G. Wu, *Small Methods*, 2020, **4**, 1900821.
6 S. Mukherjee, D. A. Cullen, S. Karakalos, K. Liu, H. Zhang, S. Zhao, H. Xu, K. L. More, G. Wang and G. Wu, *Nano Energy*, 2018, **48**, 217–226.
7 Y. Zhao, B. P. Setzler, J. Wang, J. Nash, T. Wang, B. Xu and Y. Yan, *Joule*, 2019, **3**, 2472–2484.
8 H. Xu, K. Ithisuphalap, Y. Li, S. Mukherjee, J. Lattimer, G. Soloveichik and G. Wu, *Nano Energy*, 2020, **69**, 104469.
9 O. Siddiqui and I. Dincer, *Energy*, 2019, **169**, 914–923.
10 Y. Aoki, T. Yamaguchi, S. Kobayashi, D. Kowalski, C. Zhu and H. Habazaki, *Glob. Chall.*, 2018, **2**, 1700088.

11 N. M. Adli, H. Zhang, S. Mukherjee and G. Wu, *J. Electrochem. Soc.*, 2018, **165**, J3130–J3147.
12 J. A. Herron, P. Ferrin and M. Mavrikakis, *J. Phys. Chem. C*, 2015, **119**, 14692–14701.
13 Y. Li, X. Li, H. Pillai, J. Lattimer, N. Mohd Adli, S. G. Karakalos, M. Chen, L. Guo, H. Xu, J. Yang, D. Su, H. Xin and G. Wu, *ACS Catal.*, 2020, **10**, 3945–3957.
14 N. J. Bunce and D. Bejan, *Electrochim. Acta*, 2011, **56**, 8085–8093.
15 J. Zhu, X. Zheng, J. Wang, Z. Wu, L. Han, R. Lin, H. L. Xin and D. Wang, *J. Mater. Chem. A*, 2015, **3**, 22129–22135.
16 J. Jiang, *Electrochem. Commun.*, 2017, **75**, 52–55.
17 Y. Katayama, T. Okanishi, H. Muroyama, T. Matsui and K. Eguchi, *J. Phys. Chem. C*, 2015, **119**, 9134–9141.
18 Y. Long, S. Song, J. Li, L. Wu, Q. Wang, Y. Liu, R. Jin and H. Zhang, *ACS Catal.*, 2018, **8**, 8506–8512.
19 Q. Tan, C. Shu, J. Abbott, Q. Zhao, L. Liu, T. Qu, Y. Chen, H. Zhu, Y. Liu and G. Wu, *ACS Catal.*, 2019, **9**, 6362–6371.
20 Y. He, S. Hwang, D. A. Cullen, M. A. Uddin, L. Langhorst, B. Li, S. Karakalos, A. J. Kropf, E. C. Wegener, J. Sokolowski, M. Chen, D. Myers, D. Su, K. L. More, G. Wang, S. Litster and G. Wu, *Energy Environ. Sci.*, 2019, **12**, 250–260.
21 X. X. Wang, S. Hwang, Y.-T. Pan, K. Chen, Y. He, S. Karakalos, H. Zhang, J. S. Spendelow, D. Su and G. Wu, *Nano Lett.*, 2018, **18**, 4163–4171.
22 X. X. Wang, D. A. Cullen, Y.-T. Pan, S. Hwang, M. Wang, Z. Feng, J. Wang, M. H. Engelhard, H. Zhang, Y. He, Y. Shao, D. Su, K. L. More, J. S. Spendelow and G. Wu, *Adv. Mater.*, 2018, **30**, 1706758.
23 R. Abbasi, B. P. Setzler, S. Lin, J. Wang, Y. Zhao, H. Xu, B. Pivovar, B. Tian, X. Chen, G. Wu and Y. Yan, *Adv. Mater.*, 2019, **31**, 1805876.
24 N. Daelman, M. Capdevila-Cortada and N. Lopez, *Nat. Mater.*, 2019, **18**, 1215–1221.
25 Y. Katayama, T. Okanishi, H. Muroyama, T. Matsui and K. Eguchi, *ACS Catal.*, 2016, **6**, 2026–2034.
26 Z. Qiao, S. Hwang, X. Li, C. Wang, W. Samarakoon, S. Karakalos, D. Li, M. Chen, Y. He, M. Wang, Z. Liu, G. Wang, H. Zhou, Z. Feng, D. Su, J. S. Spendelow and G. Wu, *Energy Environ. Sci.*, 2019, **12**, 2830–2841.
27 J. Li, H. Zhang, W. Samarakoon, W. Shan, D. A. Cullen, S. Karakalos, M. Chen, D. Gu, K. L. More, G. Wang, Z. Feng, Z. Wang and G. Wu, *Angew. Chem., Int. Ed.*, 2019, **58**, 18971–18980.
28 Y. Zhou, J. Yang, C. Zhu, D. Du, X. Cheng, C. H. Yen, C. M. Wai and Y. Lin, *ACS Appl. Mater. Interfaces*, 2016, **8**, 25863–25874.
29 J. Li, S. Sharma, X. Liu, Y.-T. Pan, J. S. Spendelow, M. Chi, Y. Jia, P. Zhang, D. A. Cullen, Z. Xi, H. Lin, Z. Yin, B. Shen, M. Muzzio, C. Yu, Y. S. Kim, A. A. Peterson, K. L. More, H. Zhu and S. Sun, *Joule*, 2019, **3**, 124–135.
30 J. Jiang, W. Ding, W. Li and Z. Wei, *Chem*, 2019, **6**, 1–17.
31 C. Zhong, J. Liu, Z. Ni, Y. Deng, B. Chen and W. Hu, *Sci. China Mater.*, 2014, **57**, 13–25.
32 H. Yang, S. J. Bradley, A. Chan, G. I. Waterhouse, T. Nann, P. E. Kruger and S. G. Telfer, *J. Am. Chem. Soc.*, 2016, **138**, 11872–11881.
33 K. Ding, D. A. Cullen, L. Zhang, Z. Cao, A. D. Roy, I. N. Ivanov and D. Cao, *Science*, 2018, **362**, 560–564.
34 Y. Li, J. Yang, Y. Zhou, N. Zhao, W. Zeng and W. Wang, *Colloids Surf., A*, 2017, **512**, 93–100.
35 L. Nie, D. Mei, H. Xiong, B. Peng, Z. Ren, X. I. P. Hernandez, A. DeLaRiva, M. Wang, M. H. Engelhard, L. Kovarik, A. K. Datye and Y. Wang, *Science*, 2017, **358**, 1419–1423.
36 H. Zhang, H. T. Chung, D. A. Cullen, S. Wagner, U. I. Kramm, K. L. More, P. Zelenay and G. Wu, *Energy Environ. Sci.*, 2019, **12**, 2548–2558.
37 Y. Li, Y. Zhou, C. Zhu, Y. H. Hu, S. Gao, Q. Liu, X. Cheng, L. Zhang, J. Yang and Y. Lin, *Catal. Sci. Technol.*, 2018, **8**, 5325–5333.
38 Y. Li, Y. Zhou, H. Wen, J. Yang, C. Maouche, Q. Liu, Y. Wu, C. Cheng, J. Zhu and X. Cheng, *Dalton Trans.*, 2018, **47**, 14992–15001.
39 Y. Li, H. Wen, J. Yang, Y. Zhou and X. Cheng, *Carbon*, 2019, **142**, 1–12.
40 G. H. Gunasekar, K. Park, V. Ganesan, K. Lee, N.-K. Kim, K.-D. Jung and S. Yoon, *Chem. Mater.*, 2017, **29**, 6740–6748.
41 H. Zhang, P. An, W. Zhou, B. Y. Guan, P. Zhang, J. Dong and X. W. Lou, *Sci. Adv.*, 2018, **4**, eaao6657.
42 M. Soorholtz, L. C. Jones, D. Samuelis, C. Weidenthaler, R. J. White, M.-M. Titirici, D. A. Cullen, T. Zimmermann, M. Antonietti, J. Maier, R. Palkovits, B. F. Chmelka and F. Schüth, *ACS Catal.*, 2016, **6**, 233–2340.
43 L. Song, Z. Liang, Z. Ma, Y. Zhang, J. Chen, R. R. Adzic and J. X. Wang, *J. Electrochem. Soc.*, 2018, **165**, J3095–J3100.
44 A. Estejab and G. G. Botte, *Comput. Theor. Chem.*, 2016, **1091**, 31–40.
45 A. Estejab and G. G. Botte, *Mol. Catal.*, 2018, **445**, 279–292.
46 Y. T. Chan, K. Siddharth and M. Shao, *Nano Res.*, 2020, **13**, 1920–1927.
47 J. A. Herron, P. Ferrin and M. Mavrikakis, *J. Phys. Chem. C*, 2015, **119**, 14692–14701.
48 I. Katsounaros, T. Chen, A. A. Gewirth, N. M. Markovic and M. T. Koper, *J. Phys. Chem. Lett.*, 2016, **7**, 387–392.
49 Z.-F. Li, Y. Wang and G. G. Botte, *Electrochim. Acta*, 2017, **228**, 351–360.
50 K. Siddharth, Y. Hong, X. Qin, H. J. Lee, Y. T. Chan, S. Zhu, G. Chen, S.-I. Choi and M. Shao, *Appl. Catal., B*, 2020, **269**, 118821.
51 Y. Zhou, G. Zhang, M. Yu, J. Xu, S. Qiao, X. Cheng and F. Yang, *ChemistrySelect*, 2018, **3**, 3433–3443.
52 R. H. Manso, L. Song, Z. Liang, J. X. Wang and J. Chen, *ECS Trans.*, 2018, **85**, 177–182.
53 Y. Kang, W. Wang, J. Li, C. Hua, S. Xue and Z. Lei, *Int. J. Hydrogen Energy*, 2017, **42**, 18959–18967.
54 G. Wu, N. Li, D.-R. Zhou, K. Mitsuo and B.-Q. Xu, *J. Solid State Chem.*, 2004, **177**, 3682–3692.

55 H.-Y. Sun, G.-R. Xu, F.-M. Li, Q.-L. Hong, P.-J. Jin, P. Chen and Y. Chen, *J. Energy Chem.*, 2020, **47**, 234–240.
56 H. S. Pillai and H. Xin, *Ind. Eng. Chem. Res.*, 2019, **58**, 10819–10828.
57 J. Wang, Y. Zhao, B. P. Setzler, S. Rojas-Carbonell, C. B. Yehuda, A. Amel, M. Page, L. Wang, K. Hu, L. Shi, S. Gottesfeld, B. Xu and Y. Yan, *Nat. Energy*, 2019, **4**, 392–398.
58 N. Ramaswamy and S. Mukerjee, *Chem. Rev.*, 2019, **119**, 11945–11979.
59 X. X. Wang, M. T. Swihart and G. Wu, *Nat. Catal.*, 2019, **2**, 578–589.
60 Q. Shi, Y. He, X. Bai, M. Wang, D. A. Cullen, M. Lucero, X. Zhao, K. L. More, H. Zhou, Z. Feng, Y. Liu and G. Wu, *Energy Environ. Sci.*, 2020, **13**, 3544–3555.
61 Y. He, S. Liu, C. Priest, Q. Shi and G. Wu, *Chem. Soc. Rev.*, 2020, **49**, 3484–3524.
62 J. Hou, M. Yang, C. Ke, G. Wei, C. Priest, Z. Qiao, G. Wu and J. Zhang, *Energy Chem.*, 2020, **2**, 100023.
63 A. Uddin, L. Dunsmore, H. Zhang, L. Hu, G. Wu and S. Litster, *ACS Appl. Mater. Interfaces*, 2020, **12**, 2216–2224.

